Simultaneous band-gap narrowing and carrier-lifetime prolongation of organic–inorganic trihalide perovskites

Lingping Kong[a,b], Gang Liu[a,b,1], Jue Gong[c], Qingyang Hu[a,b], Richard D. Schaller[d], Przemyslaw Dera[e], Dongzhou Zhang[e], Zhenxian Liu[b], Wenge Yang[a,b], Kai Zhu[f], Yuzhao Tang[g], Chuanyi Wang[h], Su-Huai Wei[i], Tao Xu[c,1], and Ho-kwang Mao[a,b,1]

[a]Center for High Pressure Science and Technology Advanced Research, Shanghai 201203, China; [b]Geophysical Laboratory, Carnegie Institution of Washington, Washington, DC 20015; [c]Department of Chemistry and Biochemistry, Northern Illinois University, DeKalb, IL 60115; [d]Center for Nanoscale Materials, Argonne National Laboratory, Argonne, IL 60439; [e]Hawai'i Institute of Geophysics and Planetology, School of Ocean and Earth Science and Technology, University of Hawai'i at Manoa, Honolulu, HI 96822; [f]Chemistry and Nanoscience Center, National Renewable Energy Laboratory, Golden, CO 80401; [g]National Center for Protein Science Shanghai, Institute of Biochemistry and Cell Biology, Shanghai Institutes for Biological Sciences, Chinese Academy of Sciences, Shanghai 201210, China; [h]Xinjiang Technical Institute of Physics and Chemistry, Chinese Academy of Sciences, Urumqi 830011, China; and [i]Beijing Computational Science Research Center, Beijing 100193, China

The organic–inorganic hybrid lead trihalide perovskites have been emerging as the most attractive photovoltaic materials. As regulated by Shockley–Queisser theory, a formidable materials science challenge for improvement to the next level requires further band-gap narrowing for broader absorption in solar spectrum, while retaining or even synergistically prolonging the carrier lifetime, a critical factor responsible for attaining the near-band-gap photovoltage. Herein, by applying controllable hydrostatic pressure, we have achieved unprecedented simultaneous enhancement in both band-gap narrowing and carrier-lifetime prolongation (up to 70% to ∼100% increase) under mild pressures at ∼0.3 GPa. The pressure-induced modulation on pure hybrid perovskites without introducing any adverse chemical or thermal effect clearly demonstrates the importance of band edges on the photon–electron interaction and maps a pioneering route toward a further increase in their photovoltaic performance.

perovskite | solar cell | high pressure | band gap | carrier lifetime

Methylammonium (MA) lead iodide (MAPbI$_3$) perovskite has emerged as a phenomenal photovoltaic material with power-conversion efficiency increasing from 3.8% (1) in 2009 to 22.1% (2) in 2016, along with its ease of fabrication, low cost of compositional precursors, and solution processability (1–14). The remarkable photovoltaic performance is attributed to its strong and broad (up to ∼800 nm) light absorption (10), as well as the long diffusion lengths facilitated by its extraordinarily long carrier lifetimes (∼100 ns in thin film) despite its modest mobility (11, 12, 15, 16). To further approach the Shockley–Queisser limit (17, 18), it is highly desirable to tune the crystal structure of perovskite in the way that can synergistically narrow down the band gap for broader solar spectrum absorption (10) and prolong carrier lifetime for greater photovoltage (7, 11, 12, 15, 16). However, compositional modification suffers from challenges, such as the largely shortened carrier lifetime (∼50 ps), and thus considerable loss of photovoltage upon the replacement of Pb by Sn (5, 19), or the largely widened band gap, and thus low photocurrent when I is substituted with Br or Cl (16). It also has been demonstrated that using formamidinium (FA) cations instead of MA cations in organic–inorganic perovskite materials narrows down the band gap; however, a shorter carrier lifetime is generated inevitably (20). In fact, to date, there is no reported method for simultaneously achieving band-gap narrowing and carrier-lifetime prolongation for MAPbI$_3$.

Nonetheless, the chance is to rescrutinize the band structure of MAPbI$_3$. The relatively long carrier lifetimes of 10^2 to ∼10^3 ns observed in MAPbI$_3$ single crystals originate from their unique defect physics (21). First-principles calculations demonstrated that the readily formed point defects such as interstitial MA ions and/or Pb vacancies create shallow states with trap energy less than 0.05 eV below the conduction band minimum (CBM), or above the valence band maximum (VBM), rather than detrimental deep traps at the

middle of the forbidden zone, which typically lead to non-radiative recombination (21). The uneven distribution of the trap states has been identified further by in-depth electronic characterization of MAPbI$_3$ perovskite single crystals, concluding that the traps are close to the conduction and the valence band edges (22). These theoretical and experimental results clearly indicate the importance of the band-gap modification, especially in the band-edge regions, in both light harvest and carrier dynamics. Thus, there lies an opportunity to simultaneously narrow the band gap and prolong the carrier lifetime by bringing the band edge even closer to the subgap traps, thus to position these traps even shallower to synergistically improve carrier lifetime.

As a powerful and clean tool for continuously tuning the crystal lattice and electronic wave functions (23–27), hydrostatic pressure is applied to precisely modulate the crystal lattice of perovskites and pinpoint their electronic behaviors with atomic-level understanding. The compressed perovskites exhibited a notable red-shift of its absorption edge under a very mild pressure of ∼0.3 GPa. More strikingly, the corresponding band-gap narrowing triggered a 70% to ∼100% increase in carrier lifetime. These results provide vital mechanistic guidelines for designing better photovoltaic materials.

Significance

The emergence of organic–inorganic hybrid lead triiodide perovskite materials promises a low-cost and high-efficiency photovoltaic technology. Although the high-power conversion efficiency of this technology has been successfully demonstrated, further improvement appears to be limited without further narrowing the band gap while also retaining or even synergistically prolonging the carrier lifetime. We report a synergistic enhancement in both band gap narrowing and carrier-lifetime prolongation (up to 70% to ∼100% increase) of organic–inorganic hybrid lead triiodide perovskite materials under mild pressures below ∼0.3 GPa. This work could open new territory in materials science, and new materials could be invented using the experimental and theoretical guidelines we have established herein.
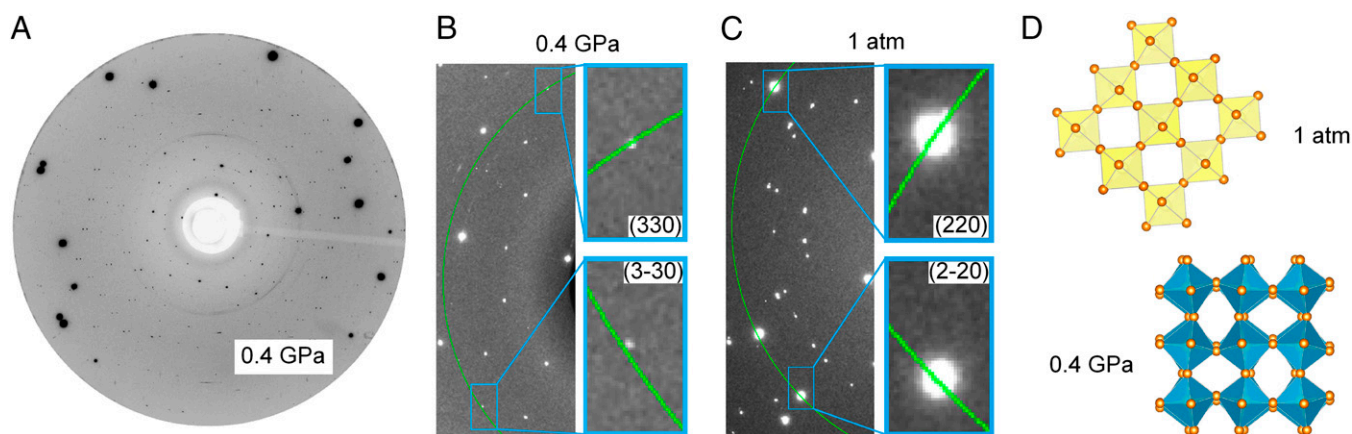
Fig. 1. Pressure-driven structural evolution of MAPbI$_3$ single crystal. (*A*) MAPbI$_3$ single-crystal diffraction pattern at 0.4 GPa at the center detector position. (*B* and *C*) Zoomed-in views of MAPbI$_3$ single-crystal diffraction patterns at 0.4 GPa and 1 atm, respectively. We can see an obvious peak splitting between (330) and (3-30) Bragg reflections at 0.4 GPa in *B*, demonstrating a symmetry lowering compared with the tetragonal phase at ambient pressure. As expected, no splitting was observed for (220) and (2-20) Bragg peaks at 1 atm in *C*, consistent with the tetragonal nature. (*D*) Pb-I inorganic frameworks of MAPbI$_3$ at 1 atm and 0.4 GPa, from which smaller Pb–I–Pb bond angles are observed at 0.4 GPa owing to the significantly distorted PbI$_6$ octahedra.

Results and Discussion

We first studied the pressure-driven phase transition of MAPbI$_3$ single crystals, which provided us atomic-level understanding of the materials structures needed for their effect on band-gap and carrier properties. The difference in structures before and after phase transition is too subtle to be fully resolved by powder X-ray diffraction (XRD) analysis; thus, the single-crystal XRD technique is used. At ambient pressure, single-crystal XRD analysis of perovskite crystals suggested a tetragonal *I4/mcm* symmetry phase (*SI Appendix, SI Section 1*), in good agreement with previous results (28). The single-crystal diffraction pattern changed significantly upon pressure increase to 0.4 GPa, demonstrating an essential phase transition from *I4/mcm* to *Imm2* (Fig. 1*A* and *SI Appendix, SI Section 2*) and corresponding to a symmetry lowering from tetragonal to orthorhombic (Fig. 1 *B* and *C*). According to the refinement results, the geometry of the polyhedra in the *Imm2* phase became obviously distorted, with the obvious smaller Pb–I–Pb bond angles ranging from 144.0° to 162.0°, in contrast to the much more regular polyhedra with a predominant bond angle of 180° in the ambient phase. Consequently, in the high-pressure phase, the voids between the octahedral that are occupied by MA ions are notably elongated under pressure (Fig. 1*D*). Pressure-driven structural evolution can be further supported by in situ high-pressure Raman and mid-infrared (IR) measurements (*SI Appendix, SI Sections 3* and *4*).

The compression changes the lattice structure of MAPbI$_3$, and subsequently redefines the boundary conditions for the electronic wave functions; thus, its optoelectronic properties are inevitably impacted, as evidenced by band-gap narrowing (Fig. 2 and *SI Appendix, SI Section 5*). We estimated the band gap of MAPbI$_3$ by extrapolating the linear portion of the $(\alpha d h v)^2$ versus hv curve in direct band-gap Tauc plots (29) (Fig. 2 *A–F*), where α is the absorption coefficient, d is the sample thickness, and hv is photon energy. At ambient pressure, the band-gap magnitude was determined to be 1.537 eV (Fig. 2*A*), consistent with reported results (30). Remarkably, as the pressure increases, the band gap of MAPbI$_3$ undergoes a noticeable red-shift to 1.507 eV at 0.32 GPa (Fig. 2*C*). The mechanistic understanding of the pressure-driven band-gap evolution can be elucidated by considering the inverted band nature of MAPbI$_3$ perovskite (30). The band gap is determined by change of VBM and CBM. We recognize that the difference in electronegativity between Pb and I is relatively small (Pb: 2.33 vs. I: 2.66), giving rise to the strong hybridization of the Pb s and I p antibonding character in VBM, whereas the CBM has

mostly a nonbonding Pb p character (21, 30). Note that as the pressure increases in low-pressure phase, the predominant Pb–I–Pb bond angle remains at nearly 180°, but the bond length shortens under pressure (Fig. 2*J*). As such, the Pb s and I p orbital coupling enhances and pushes up the VBM. The CBM is mostly a nonbonding localized state of Pb p orbitals, which is not sensitive to bond length or pressure. Therefore, under pressure, the band gap decreases and most of the change comes from the VBM. The pressure-induced red-shift and subsequent "blue jump" (Fig. 2*D*) of the band gap for MAPbI$_3$ can be reproduced successfully by first-principles calculations (Fig. 2 *H* and *I* and *SI Appendix, SI Section 6*).

It is worth mentioning that if the crystal could have been retained in the *I4/mcm* phase, the calculated band-gap narrowing upon pressure-induced bond-length shrinkage could reach the optimized value of 1.3 to 1.4 eV, achieving the Shockley–Queisser limit, at which the energy-conversion efficiency of solar cells is up to 33% (15). We expect such band-gap values can be realized at relatively low pressure ranges, between 1.0 and 1.5 GPa at room temperature, if the phase transition can be properly inhibited through further intelligent materials design and/or device engineering.

The blue jump (Fig. 2*D*) can be understood from the fact that the averaged Pb–I–Pb bond angle in *Imm2* [i.e., the high-pressure orthorhombic phase] is 154.6° (*SI Appendix, SI Section 2*), which is considerably smaller than that (171.8°) in *I4/mcm* [i.e., the low-pressure tetragonal phase (31)]. Therefore, when phase transition occurs, the Pb-I bond is partially broken and the Pb s and I p orbital coupling is reduced, as illustrated in Fig. 2*K*, leading to widened band gap.

Previous work suggests that the dominant trap states are located in the shallow energy near CBM and VBM, which protects the electron–hole pair against recombination (21, 22). Thus, the demonstrated band edges approaching (Fig. 2) should play a critical role in carrier properties. For the first time, to our knowledge, we carried out in situ high-pressure time-resolved photoluminescence (TRPL) measurements for hybrid perovskites to study the pressure influence on the carrier lifetime τ (Fig. 3), a decisive quantity responsible for the materials' photovoltaic performance. Because the photoluminescence (PL) decay dynamics in perovskite crystals greatly depends on the defect states formed during the crystal growth, it is inevitable to see the variation in carrier lifetime among different samples. Therefore, our measurement was conducted on the same piece of MAPbI$_3$ single-crystal sample upon compression
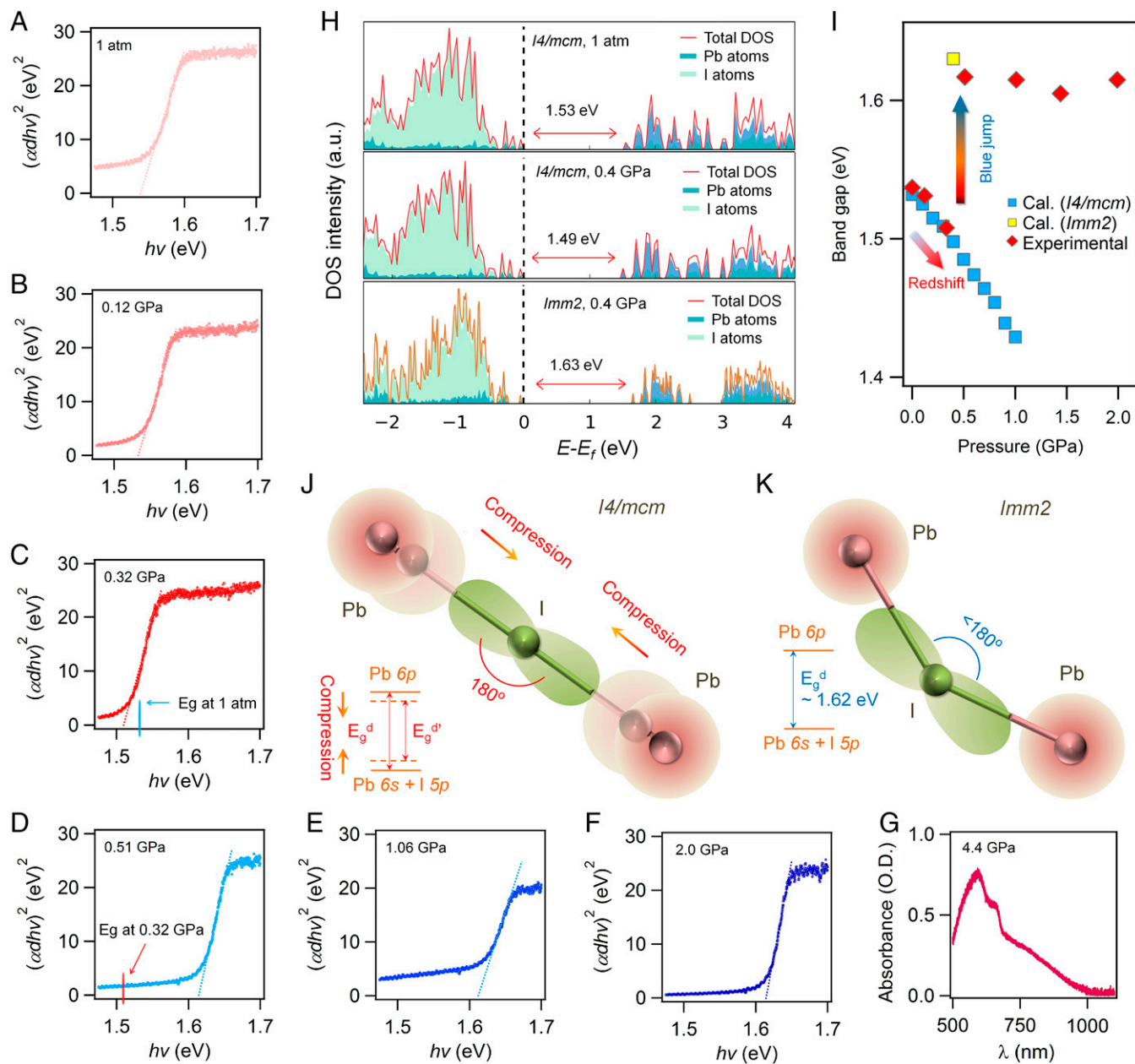
Fig. 2. Realization of band edges approaching in MAPbI$_3$ single crystal upon compression. (*A–F*) Direct band-gap Tauc plots for MAPbI$_3$ single crystals at 1 atm, 0.12 GPa, 0.32 GPa, 0.51 GPa, 1.06 GPa, and 2.0 GPa, respectively. The magnitude of band gap can be determined by extrapolating the linear portion of the Tauc plot to the baseline. Pressure-driven red-shift of the band gap gradually occurs between 1 atm and 0.3 GPa, followed by a blue jump at 0.51 GPa, corresponding to the low-pressure and high-pressure phase ranges, respectively. (*G*) Absorption spectroscopy measured at 4.4 GPa, in which no clear onset of absorption was observed corresponding to the amorphous nature. (*H*) Density of states (DOS) of MAPbI$_3$ with a structure of *I4/mcm* at 1 atm (*Top*), *I4/mcm* at 0.4 GPa (*Middle*), and *Imm2* at 0.4 GPa (*Bottom*). Clearly, our calculations reproduced the red-shift and blue jump, as evidenced by the band-gap values of 1.53, 1.49, and 1.63 eV, respectively. (*I*) Pressure-driven band-gap evolution of MAPbI$_3$. Band edges approaching was realized in a low-pressure phase range. (*J* and *K*) Schematic models of the red-shift and blue jump, respectively. For the *I4/mcm* phase, as pressure increased, the dominated Pb–I–Pb bond angle kept 180° and the electron wave function overlapped more; thus, the bandwidth of both the valance band and the conduction band expanded. For the *Imm2* phase, the Pb–I–Pb bond angle became much smaller than 180° and the electron wave function overlapped much less than that in the *I4/mcm* phase.

(Fig. 3 *A–F*). We then performed biexponential fitting as $I_{PL}(t) = I_{int}[\alpha \cdot \exp(-t/\tau_1) + \beta \cdot \exp(-t/\tau_2) + I_0]$ on all time-resolved traces to quantify the PL decay dynamics reflected by the slow-decay component τ_1 and the fast-decay component τ_2, which are assigned to free carrier recombination in the bulk and surface effect, respectively (7). At ambient pressure, our single-crystal sample exhibits a superposition of slow and fast dynamics, on the order of $\tau_1 = 425 \pm 10$ ns and $\tau_2 = 8\pm2$ ns (Fig. 3*A*), respectively, which are comparable to the reported values (32). Astonishingly, at a very mild pressure of 0.1

GPa, the MAPbI$_3$ single crystal exhibits a phenomenal rise in carrier lifetime of $\tau_1 = 658 \pm 12$ ns and $\tau_2 = 14 \pm 2$ ns (Fig. 3*B*), over 50% longer than that under ambient pressure. The carrier lifetime reaches a "peak" value of $\tau_1 = 715 \pm 15$ ns and $\tau_2 = 14 \pm 2$ ns at 0.3 GPa (Fig. 3*D*), above which the phase transition occurs. It is also noted that the pressure at which the peak value of carrier lifetime is obtained is nearly exactly in line with the pressure where the narrowest band gap is obtained (0.32 GPa; Fig. 2*C*). In particular, because the relative contribution of the bulk-dominated slow component to the static PL
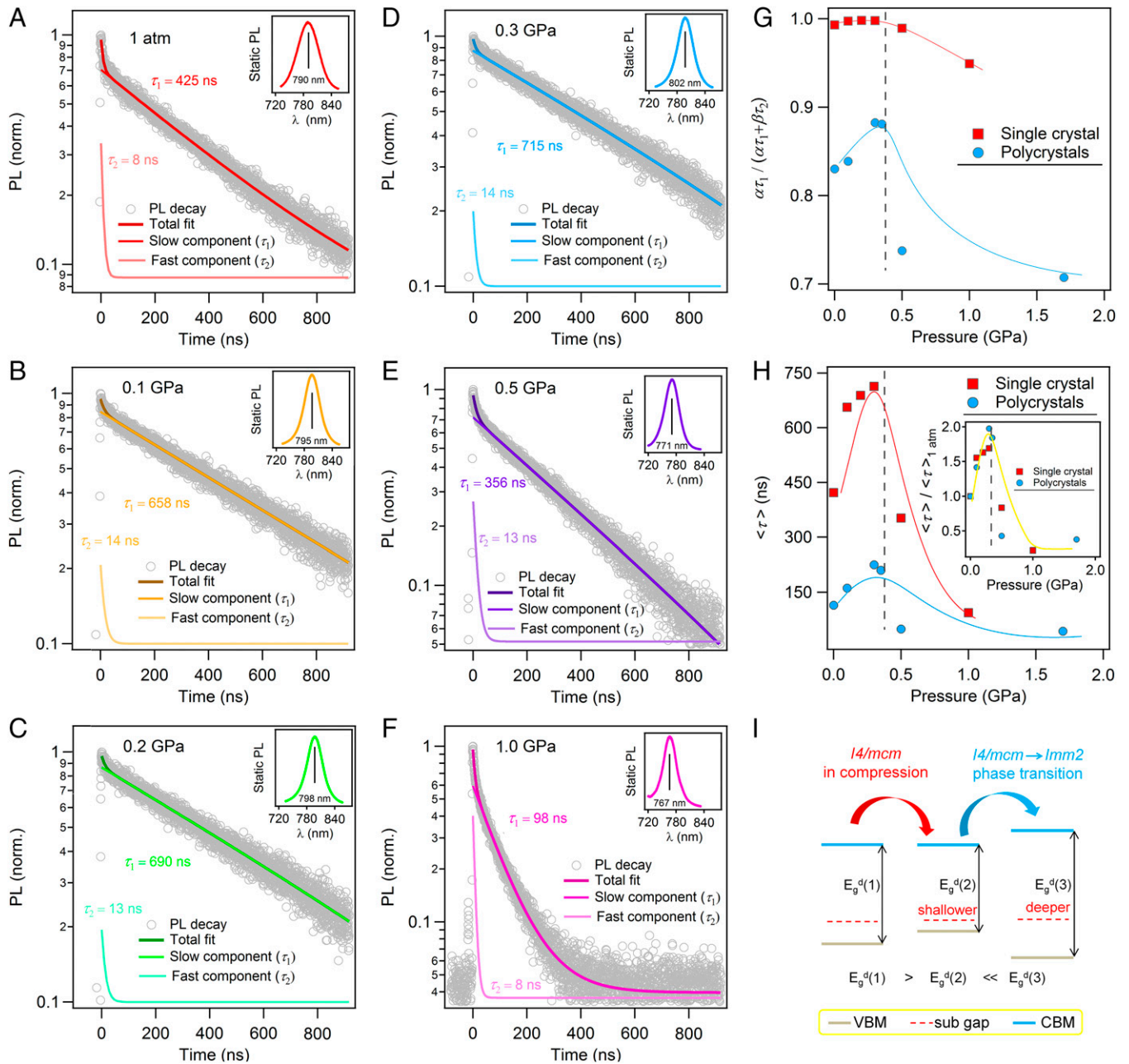
Fig. 3. Significant carrier-lifetime prolongation of MAPbI$_3$ upon compression. (*A–F*) In situ high-pressure TRPL measurements on a MAPbI$_3$ single crystal at 1 atm (*A*), 0.1 GPa (*B*), 0.2 GPa (*C*), 0.3 GPa (*D*), 0.5 GPa (*E*), and 1.0 GPa (*F*). *Insets* in *A–F* show the static PL signal at respective pressures. From the static PL spectra, main peaks were clearly identified and the respective TRPLs were measured from their wavelengths. For all measured pressures, both slow and fast components of carrier lifetime were determined using biexponential fittings ($I_{PL}(t) = I_{int}[\alpha \cdot \exp(-t/\tau_1) + \beta \cdot \exp(-t/\tau_2) + I_0]$) on time-decay traces and denoted as τ_1 and τ_2, respectively, as shown in *A–F*. (*G*) Pressure dependence of the relative contribution of the bulk-dominated slow component, $\alpha\tau_1/(\alpha\tau_1+\beta\tau_2)$, for both MAPbI$_3$ single-crystal and polycrystals samples. (*H*) Pressure dependence of the mean carrier lifetime, $<\tau> = [\alpha\tau_1/(\alpha\tau_1+\beta\tau_2)]\tau_1 + [\beta\tau_2/(\alpha\tau_1 + \beta\tau_2)]\tau_2$, for both MAPbI$_3$ single-crystal and polycrystal samples. Peak values in carrier lifetimes of MAPbI$_3$ were observed at 0.3 GPa. (*H, Inset*) A normalized result. Compared with the values of $<\tau>$ measured at 1 atm, dramatic increases of ~70% and ~100% were observed at 0.3 GPa for single crystals and polycrystals, respectively. (*I*) Schematic of the correlation between band edges approaching and carrier-lifetime prolongation. As the band gap narrows, the subgap states closing to band edges will be shallower; thus, lower trap states can be expected.

[defined as $\alpha\tau_1/(\alpha\tau_1+\beta\tau_2)$] also reaches a peak value of ~0.99 at 0.3 GPa (Fig. 3*G*), it is reasonable to state that the pressure-enhanced carrier lifetime must originate from the structural change of the bulk of the crystal.

Because polycrystalline MAPbI$_3$ is the actual form in perovskite-based thin film solar cells, we also conducted an in situ high-pressure TRPL study on MAPbI$_3$ polycrystals to verify the repeatability of the pressure-induced carrier lifetime evolution

(*SI Appendix, SI Section 7*). It is understandable that the polycrystalline sample exhibits a much shorter carrier lifetime than their single-crystal counterparts because of their greater structural defective states and faster trap-induced recombination rate (7, 30). Nevertheless, the pressure-enhanced carrier lifetime reappears and reaches a peak value of ~225 ns, along with the peak contribution of ~0.88 from the slow component at 0.3 GPa (Fig. 3 *G* and *H* and *SI Appendix, SI Section 7*),

APPLIED PHYSICAL SCIENCES
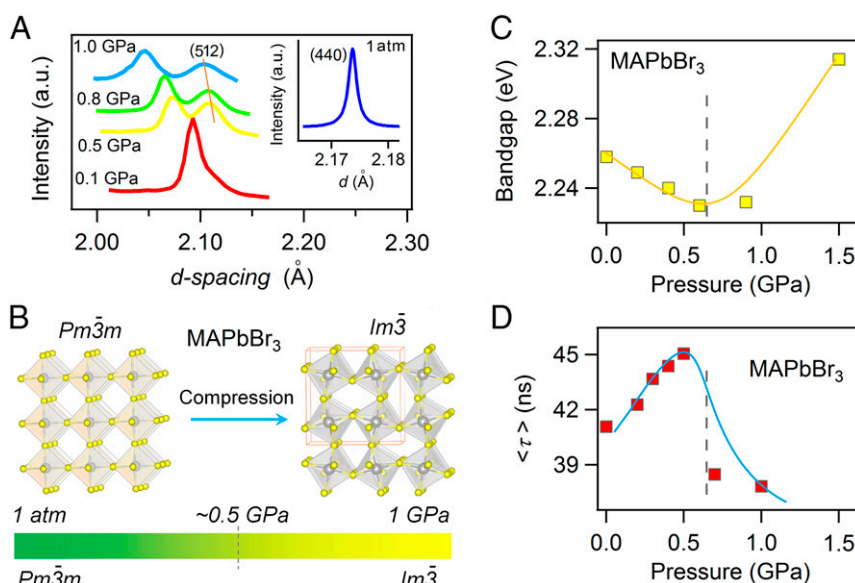
Fig. 4. Pressure-driven evolution of structure, electronic band, and carrier property in MAPbBr$_3$. (*A*)Selected high-pressure synchrotron powder XRD profiles of MAPbBr$_3$ from 1 atm to 1 GPa. A high-pressure phase with an $Im\bar{3}$ space group can be ascertained by the occurrence of (512) reflection that is absent at 1 atm (*Inset*). Detailed GSAS fittings are available in *SI Appendix, SI Section 2*. (*B*) Pb-Br inorganic frameworks of MAPbBr$_3$ for low-pressure $Pm\bar{3}m$ and high-pressure $Im\bar{3}$ phases. Similar to MAPbI$_3$, the high-pressure phase in MAPbBr$_3$ also exhibits the characteristic elongation of the lead–halide octahedral, together with smaller lead–halide–lead bond angles. (*C* and *D*) Demonstration of the band-gap narrowing and carrier-lifetime prolongation in MAPbBr$_3$ at mild pressures, respectively. Gray dash lines in *C* and *D* indicate the approximate phase boundaries. Yellow (in *C*) and blue (in *D*) dashed lines guide the eyes to the peak phenomenon.

seamlessly matching what we observed from the single-crystal study. Considering the relative contribution of slow and fast components, we evaluated the mean carrier lifetime as $<\tau> = [\alpha\tau_1/(\alpha\tau_1+\beta\tau_2)]\tau_1 + [\beta\tau_2/(\alpha\tau_1 + \beta\tau_2)]\tau_2$ for both the single-crystal and polycrystalline samples (Fig. 3*H*). An increase in $<\tau>$ by 70% and 100% can be demonstrated in single-crystal and polycrystalline samples, respectively. Fig. 3*I* schematically elucidated the pressure-enhanced carrier lifetime. Explicitly, as pressure increases, the trap states that are already present in the subgap close to VBM become even shallower, because of the aforementioned VBM ascendance. Thus, a larger portion of recombination becomes radiative, and a longer carrier lifetime is consequently expected. Correspondingly, recalling the pressure-dependent absorption study, the MAPbI$_3$ single crystal exhibits a much sharper onset of the absorption edge at 0.32 GPa (Fig. 2*C*) than that at ambient pressure conditions (Fig. 2*A*), indicating the absence of deep trap states and likely the smaller offset between the band gap and attainable open-circuit voltage of the solar cell device (30, 33, 34). For the high-pressure phase, the relatively larger band gap of ~1.62 eV leads to deep trap states; therefore, a significant drop in lifetime can be observed (Fig. 3 *E*, *F*, and *H*).

To generalize our observations, we further explored the pressure effect on MAPbBr$_3$ perovskite. Our in situ high-pressure XRD results revealed that the MAPbBr$_3$ undergoes a cubic–cubic phase transition from $Pm\bar{3}m \rightarrow Im\bar{3}$ occurring at ~0.5 GPa (Fig. 4*A*) (35). This phase transition appears as the distortion of the PbBr$_3^-$ polyhedral framework and the decrease in the Pb-Br-Pb bond angle (Fig. 4*B*). Echoing MAPbI$_3$, the narrowest band gap of ~2.230 eV (Fig. 4*C*), together with the longest carrier lifetime (Fig. 4*D*), also appears around the phase-transition pressure, ~0.5–0.6 GPa. Our findings have clearly demonstrated the usefulness of pressure-driven modulation on crystal structures that leads to a desirable improvement in material properties.

Conclusions

Organic–inorganic lead trihalide perovskites under pressure exhibit an unprecedented simultaneous occurrence of band-gap narrowing and carrier-lifetime prolongation, both of which are exceptionally desirable trends for achieving better photovoltaic performance than the current state of the art. Additionally, the pressure-driven $I4/mcm \rightarrow Imm2$ phase transition in MAPbI$_3$, which is identified in this work for the first time, to our knowledge, is another crucial factor that alters the electron-density function between Pb and I atoms via the change of bond angles. Our discoveries map a prosperous route toward better materials-by-design under practical conditions, because the very mild pressures (<1 GPa) where the optimized functionalities appear, is much lower than the current technique limit for generating hydrostatic pressure (36), and the mediate lattice shrinking can be readily achieved through routine substrate engineering in thin films technologies (37). We conclude that even for the hybrid perovskites with a single material composition, there is a considerable tunability in their properties that can fit them to a variety of applications requiring modulated band gaps and long carrier lifetime, such as solar cells as well as other optoelectronic systems.

Materials and Methods

In situ synchrotron high-pressure powder and single-crystal XRD experiments were carried out at the 13 BM-C of the Advanced Photon Source (APS), Argonne National Laboratory (ANL). A monochromatic X-ray with a wavelength of 0.434 Å was used, and the incident X-ray beam was focused to a 15- × 15-μm spot. Silicon oil was used as pressure-transmitting medium. Two ruby balls with diameters on the order of 10 μm were loaded in the sample chamber. The pressure was determined by the ruby luminescence method. The GSAS program was used to refine the obtained experimental powder XRD profiles. For single-crystal experiments, diffraction images were analyzed using the ATREX/RSV software package.

In situ high-pressure Raman measurements were conducted at the Center for High Pressure Science and Technology Advanced Research (HPSTAR), Shanghai. The micro-Raman system is based on an optical microscope (Renishaw microscope, equipped with 5×, 20×, 50×, and 100× short and long working distance microscope objectives) used to focus the excitation light, an inVia Renishaw microscope, and a standard CCD array detector.

In situ high-pressure optical absorption spectroscopy was conducted at the experimental station U2A beamline of the National Synchrotron Light Source (NSLS) at Brookhaven National Laboratory (BNL). The visible absorption measurements between 10,000 and 25,000 cm^{-1} used a customized visible microscope system, whereas the near-IR measurements between 8,000 and 11,000 cm^{-1} used a

Bruker Vertex 80v FT-IR spectrometer coupled to a Hyperion-2000 microscope with a MCT detector and CaF_2 beam splitter. A symmetric type diamond anvil cell (DAC) and a pair of IIa-type diamond anvils with the culets size of 300 μm were used. KBr was used as pressure transmitting medium and the KBr spectra were used to determine an absorbance baseline.

In situ high-pressure photoluminescence measurement was conducted at the Center for Nanoscale Materials (CNM), ANL. To measure static photoluminescence and time-resolved photoluminescence dynamics, single-crystal and polycrystalline samples were photoexcited at 450 nm and 40 nJ/cm^2 via a 35-ps pulse-width laser diode. PL photons were collected with a lens and directed to a 300-mm focal-length grating spectrograph outfitted with a thermoelectrically cooled CCD and avalanche photodiode with time-correlated single-photon-counting electronics. The sample was loaded in a Mao-type symmetric DAC with a pair of 400-μm culets and placed in a rhenium (Re) gasket hole with a diameter on the order of 200 μm. Silicon oil was used as pressure-transmitting medium, which provided good chemical inertness and hydrostatic conditions.

For detailed information about materials and experimental methods, see *SI Appendix, SI Materials and Methods*.

1. Kojima A, Teshima K, Shirai Y, Miyasaka T (2009) Organometal halide perovskites as visible-light sensitizers for photovoltaic cells. *J Am Chem Soc* 131(17):6050–6051.
2. National Renewable Energy Laboratory (2016) Best Research-Cell Efficiencies, NREL Research Cell Efficiency Records (National Renewable Energy Laboratory, Golden, CO). Available at www.nrel.gov/ncpv/images/efficiency_chart.jpg. Accessed April 5, 2016.
3. Kim HS, et al. (2012) Lead iodide perovskite sensitized all-solid-state submicron thin film mesoscopic solar cell with efficiency exceeding 9%. *Sci Rep* 2:591.
4. You J, et al. (2014) Low-temperature solution-processed perovskite solar cells with high efficiency and flexibility. *ACS Nano* 8(2):1674–1680.
5. Hao F, Stoumpos CC, Cao DH, Chang RPH, Kanatzidis MG (2014) Lead-free solar-state organic-inorganic halide perovskite solar cells. *Nat Photonics* 8(6):489–494.
6. Nie W, et al. (2015) Solar cells. High-efficiency solution-processed perovskite solar cells with millimeter-scale grains. *Science* 347(6221):522–525.
7. Shi D, et al. (2015) Solar cells. Low trap-state density and long carrier diffusion in organolead trihalide perovskite single crystals. *Science* 347(6221):519–522.
8. Luo B, et al. (2015) Synthesis, optical properties, and exciton dynamics of organolead bromide perovskite nanocrystals. *J Phys Chem C* 119(47):26672–26682.
9. Li Y, et al. (2015) Fabrication of planar heterojunction perovskite solar cells by controlled low-pressure vapor annealing. *J Phys Chem Lett* 6(3):493–499.
10. Jeon NJ, et al. (2015) Compositional engineering of perovskite materials for high-performance solar cells. *Nature* 517(7535):476–480.
11. deQuilettes DW, et al. (2015) Solar cells. Impact of microstructure on local carrier lifetime in perovskite solar cells. *Science* 348(6235):683–686.
12. Zhou H, et al. (2014) Photovoltaics. Interface engineering of highly efficient perovskite solar cells. *Science* 345(6196):542–546.
13. Xing G, et al. (2014) Low-temperature solution-processed wavelength-tunable perovskites for lasing. *Nat Mater* 13(5):476–480.
14. Ganose AM, Savory CN, Scanlon DO (2015) $(CH_3NH_3)_2Pb(SCN)_2I_2$: A more stable structural motif for hybrid halide photovoltaics? *J Phys Chem Lett* 6(22):4594–4598.
15. Johnston MB, Herz LM (2016) Hybrid perovskites for photovoltaics: Charge-carrier recombination, diffusion, and radiative efficiencies. *Acc Chem Res* 49(1):146–154.
16. Brenner TM, Egger DA, Kronik L, Hodes G, Cahen D (2016) Hybrid organic-inorganic perovskites: Low-cost semiconductors with intriguing charge-transport properties. *Nat Rev Mater* 1:15007.
17. Sha WEI, Ren X, Chen L, Choy WCH (2015) The efficiency limit of $CH_3NH_3PbI_3$ perovskite solar cells. *Appl Phys Lett* 106(22):221104.
18. Shockley W, Queisser HJ (1961) Detailed balance limit of efficiency of p-n junction solar cells. *J Appl Phys* 32(3):510–519.
19. Parrott ES, et al. (2016) Effect of structural phase transition on charge-carrier lifetimes and defects in $CH_3NH_3SnI_3$ perovskite. *J Phys Chem Lett* 7(7):1321–1326.
20. Han Q, et al. (2016) Single crystal formamidinium lead iodide (FAPbI3): Insight into the structural, optical, and electrical properties. *Adv Mater* 28(11):2253–2258.
21. Yin WJ, Shi T, Yan Y (2014) Unusual defect physics in $CH_3NH_3PbI_3$ perovskite solar cell absorber. *Appl Phys Lett* 104(6):063903.
22. Adinolfi V, et al. (2016) The in-gap electronic state spectrum of methylammonium lead iodide single-crystal perovskites. *Adv Mater* 28(17):3406–3410.
23. Mao HK, Hemley RJ (1994) Ultrahigh-pressure transitions in solid hydrogen. *Rev Mod Phys* 66(2):671–692.
24. Jaffe A, et al. (2016) High-pressure single-crystal structures of 3D lead-halide hybrid perovskites and pressure effects on their electronic and optical properties. *ACS Cent Sci* 2(4):201–209.
25. Matsuishi K, Ishihara T, Onari S, Chang YH, Park CH (2004) Optical properties and structural phase transitions of lead-halide based inorganic–organic 3D and 2D perovskite semiconductors under high pressure. *Phys Status Solidi* 241(14):3328–3333.
26. Wang Y, et al. (2015) Pressure-induced phase transformation, reversible amorphization, and anomalous visible light response in organolead bromide perovskite. *J Am Chem Soc* 137(34):11144–11149.
27. Ou T, et al. (2016) Visible light response, electrical transport, and amorphization in compressed organolead iodine perovskites. *Nanoscale* 8(22):11426–11431.
28. Baikie T, et al. (2013) Synthesis and crystal chemistry of the hybrid perovskite $(CH_3NH_3)PbI_3$ for solid-state sensitised solar cell applications. *J Mater Chem A Mater Energy Sustain* 1(18):5628–5641.
29. Tauc J (1968) Optical properties and electronic structure of amorphous Ge and Si. *Mater Res Bull* 3(1):37–46.
30. Yin WJ, Yang JH, Kang J, Yan Y, Wei SH (2015) Halide perovskite materials for solar cells: A theoretical review. *J Mater Chem A Mater Energy Sustain* 3(17):8926–8942.
31. Stoumpos CC, Kanatzidis MG (2015) The renaissance of halide perovskites and their evolution as emerging semiconductors. *Acc Chem Res* 48(10):2791–2802.
32. Saidaminov MI, et al. (2015) High-quality bulk hybrid perovskite single crystals within minutes by inverse temperature crystallization. *Nat Commun* 6:7586.
33. Xiao Z, et al. (2016) Thin-film semiconductor perspective of organometal trihalide perovskite materials for high-efficiency solar cells. *Mater Sci Eng Rep* 101:1–38.
34. De Wolf S, et al. (2014) Organometallic halide perovskites: Sharp optical absorption edge and its relation to photovoltaic performance. *J Phys Chem Lett* 5(6):1035–1039.
35. Swainson IP, Tucker MG, Wilson DJ, Winkler B, Milman V (2007) Pressure response of an organic-inorganic perovskite: Methylammonium lead bromide. *Chem Mater* 19(10):2401–2405.
36. Dalladay-Simpson P, Howie RT, Gregoryanz E (2016) Evidence for a new phase of dense hydrogen above 325 gigapascals. *Nature* 529(7584):63–67.
37. Haeni JH, et al. (2004) Room-temperature ferroelectricity in strained $SrTiO_3$. *Nature* 430(7001):758–761.